Journal of
Marine Science and Engineering

MDPI

Article

Study on the Influence of Gradient Wind on the Aerodynamic Characteristics of a Two-Element Wingsail for Ship-Assisted Propulsion

Chen Li [1,2,3,*], Hongming Wang [2,3] and Peiting Sun [1]

1 Marine Engineering College, Dalian Maritime University, Dalian 116026, China
2 Marine Electrical and Intelligent Engineering College, Jiangsu Maritime Institute, Nanjing 211170, China
3 Jiangsu Ship Energy-Saving Engineering Technology Center, Nanjing 211170, China
* Correspondence: lichen0987654321@163.com

Abstract: It is well known that sail-assisted propulsion works under gradient wind conditions in the atmospheric boundary layer, and is an energy-saving device for fuel consumption. In order to study the aerodynamic characteristics of a wingsail in the atmospheric boundary layer above sea level, a transition SST turbulence model was used for numerical simulation of the wingsail with uniform and gradient wind conditions. We concluded that gradient wind conditions can delay the stall caused by an increased angle of attack. This is because the airflow on the suction surface of the wingsail in the spanwise direction exerts an acceleration towards the top of the wingsail. At the same time, supplementary airflow compresses the separated vortex, thus delaying the stall of the two-element wingsail. Under gradient wind conditions, the flow separation of the wingsail develops rapidly in the stall angles. Once a flat separation vortex is formed at the trailing edge of the wingsail, with the slow increase of flap deflection angle, flow separation rapidly expands and a deep stall occurs. Therefore, a small change of the flap deflection angle in the near-stall angles may lead to a deep stall of the wingsail, which should be avoided in engineering applications. Finally, the influence of the average speed of the gradient wind on the aerodynamic performance of the two-element wingsail was analyzed.

Keywords: two-element wingsail; energy-saving device; gradient wind; numerical simulation

check for updates

Citation: Li, C.; Wang, H.; Sun, P. Study on the Influence of Gradient Wind on the Aerodynamic Characteristics of a Two-Element Wingsail for Ship-Assisted Propulsion. *J. Mar. Sci. Eng.* **2023**, *11*, 134. https://doi.org/10.3390/jmse11010134

Academic Editors: Kourosh Koushan and Michele Viviani

Received: 24 November 2022
Revised: 14 December 2022
Accepted: 29 December 2022
Published: 6 January 2023

Copyright: © 2023 by the authors. Licensee MDPI, Basel, Switzerland. This article is an open access article distributed under the terms and conditions of the Creative Commons Attribution (CC BY) license (https://creativecommons.org/licenses/by/4.0/).

1. Introduction

In the past two years, due to the impact of the COVID-19 epidemic and the turbulent international situation, international crude oil prices have been rising and the operating costs of shipping companies have been increasing, which has prompted sail-assisted navigation technology to be further studied in many countries to reduce fuel consumption. Among them, wingsail-assisted propulsion technology has been favored by researchers due to its non-energy consumption, a wide range of available wind directions, and energy-saving effect. In 2017, AYRO of France designed Oceanwings [1], which has been proven to reduce fuel consumption of cargo ships by up to 45%, by incorporating a two-element wingsail on the BMW Oracle fleet, as shown in Figure 1. In 2018, China National Shipbuilding Group [2] delivered the world's first VLCC "Kaili," as shown in Figure 2, with wingsails, and the test results showed a considerable energy-saving effect.

In 2021 Michelin's R & D department and two Swiss inventors jointly launched the Wing Sail Mobility (WISAMO) system [3], shown in Figure 3, featuring an inflatable wingsail technology. In July 2021, Meimura Shipbuilding in Japan, together with Japanese shipowner NS United Shipping, announced another joint development of a sail-powered energy-saving system for a 183,000 dwt Cape-size bulk carrier [4], as shown in Figure 4, which presented excellent performance in the utilization of wind energy.

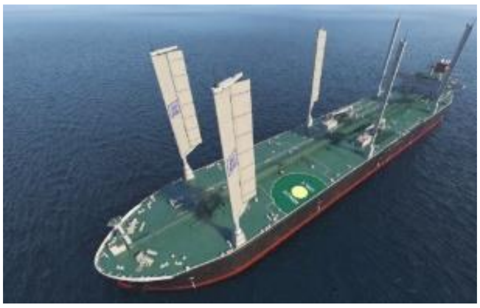

Figure 1. Oceanwings designed by AYRO.

Figure 2. Kaili ship built by the Dazhang Group.

Figure 3. Wing Sail Mobility (WISAMO) system.

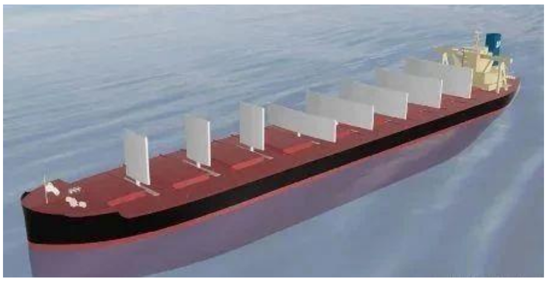

Figure 4. "Wind Challenger" developed by Mingcun shipbuilding.

As seen above, wing sails mostly work within the atmospheric boundary layer with a thickness of 0–100 m above sea level. As the wind flows over the sea surface, the airflow status is influenced by the viscous resistance of the sea surface and results in a pressure gradient within the atmospheric layer [5], in which the lower interface is mobile and involves various mechanisms of interaction between wind and wind waves. Much offshore empirical data (e.g., the results of large offshore tests such as AMTEX) have indicated the existence of significant gradient wind phenomena within a few tens of meters above the sea surface [6].

Researchers consider the wind gradient effects in the atmospheric boundary layer when studying the aerodynamic response and load characteristics of high-rise buildings [7], large bridges [8], wind machines [9], and unmanned aircraft gliding [10]. While sail-design enthusiasts, such as Daniel [11], Blakeley [12], Vincent Chapin [13], and Alessandro [14], have not considered the effect of gradient wind conditions when studying the aerodynamic characteristics of multi-element wingsails, Wenrong Hu [15] and Ian Mortimer [16] analyzed the aerodynamic performance of conventional sails under real gradient wind conditions. However, the aerodynamic load distribution and flow field of wingsails under gradient wind conditions have not been fully studied.

Usually, a linear mathematical model is used to describe the wind gradient in the atmospheric boundary layer. Thuillier and Lappe [17] introduced a roughness factor to describe the wind gradient profile. Then, Ricardo Bencatel [18] optimized a logarithmic mathematical model of wind gradient through experiments. Stevenson [19] proposed the parabolic law to describe the wind gradient profile, but it is not applicable to the atmospheric boundary layer below 10 m. Holmes [20] successfully verified the law of wind speed variation along the thickness of the atmospheric boundary layer with the help of an exponential mathematical model.

Meanwhile, some scholars have conducted in-depth studies on mathematical models of wind gradient at sea level. HW Tieleman [21] provided prediction methods for parameters such as rough elements, friction velocity, and wind gradient characteristics for the atmospheric boundary layer by wind simulation experiments based on rough element data at sea level. Bower [22] developed a wind gradient model of the sea atmospheric boundary layer and determined the gliding characteristics of a fixed-wing UAV in the wind gradient field. Li [23] established a wind gradient model for the sea surface atmospheric boundary layer and conducted a detailed study on the influence of sea surface atmospheric boundary layer and sea-air interactions.

In this study, we introduce a mathematical model of wind gradient at sea level, and analyze the aerodynamic performance and flow field of a wingsail under uniform wind and gradient wind conditions, considering the changing of angle of attack, flap deflection angle and average wind speed. The result could provide a reference for studying the effect of wind gradient on the stall of the wingsail.

2. Mathematical Model of Wind Gradient at Sea Level

Using the North-East Earth (NED) coordinate system as a standard [10], the sea-level wind field at a location $r_i = [x_i, y_i, z_i]^T$ and time t is specified as the wind speed vector U_i and gradient matrix J_{U_i}:

$$U_i = \begin{bmatrix} U_{ix}(x_i, y_i, z_i, t) \\ U_{iy}(x_i, y_i, z_i, t) \\ U_{iz}(x_i, y_i, z_i, t) \end{bmatrix} \tag{1}$$

$$J_{U_i} = \begin{pmatrix} \frac{\delta U_{ix}}{\delta x_i} & \frac{\delta U_{ix}}{\delta y_i} & \frac{\delta U_{ix}}{\delta z_i} \\ \frac{\delta U_{iy}}{\delta x_i} & \frac{\delta U_{iy}}{\delta y_i} & \frac{\delta U_{iy}}{\delta z_i} \\ \frac{\delta U_{iz}}{\delta x_i} & \frac{\delta U_{iz}}{\delta y_i} & \frac{\delta U_{iz}}{\delta z_i} \end{pmatrix} \tag{2}$$

It is assumed that the direction of wind speed in the sea level wind field points to the positive direction of the x_i axis, i.e., $U_{ix} > 0$, and the remaining components $U_{iy} = 0$, $U_{iz} = 0$. Therefore, the wind speed can be expressed by U, and its magnitude is distributed in a gradient at sea level.

2.1. Logarithmic Mathematical Model of Wind Gradient [24]

The wind speed at the sea surface is influenced by the atmospheric boundary layer and is distributed in a gradient along the spanwise height, which is influenced by two main factors: first, the frictional drag brought by the roughness of the sea level, which directly reduces the wind speed near the sea surface, and second, the vertical stability of the atmospheric boundary layer disturbed by the thermal effect of the airflow. The strong and perturbing effects of the airflow gradually decrease with height, and the variation law of this wind speed obeys the empirical theoretical formula in Prandtl turbulence.

$$U = \frac{U_0}{K} \ln\left(\frac{h}{h_0}\right) \tag{3}$$

$$U_0 = \sqrt{\frac{\tau_0}{\rho}} \tag{4}$$

where U is the wind speed at height h, and K is the Karman coefficient, which is about 0.4. U_0 is the friction velocity and τ_0 is the shear stress of the sea surface. h_0 is the roughness length parameter or roughness factor, whose value is mainly affected by factors such as wave height; the value range is generally 0.0001 m–0.01 m, and 0.001 m can be taken for moderate wind waves.

Derived from Equation (3):

$$U = U_R \frac{\ln h - \ln h_0}{\ln h_R - \ln h_0} \tag{5}$$

where U is the speed at height h, and U_R is the speed at the altitude h_R.

The gradient of wind speed relative to height can be expressed as:

$$\frac{\delta U}{\delta h} = \frac{U_R}{h \ln(h_R/h_0)} \tag{6}$$

The reference wind speed can be selected according to the reference height h_R to define the wind profile's overall gradient and average speed value. Generally, the wind speed at 10 m is selected as the reference wind speed, as shown in Figure 5. The mathematical model of wind gradient is shown, whose roughness factor h_0 changes with surface roughness and other factors, as in Figure 6.

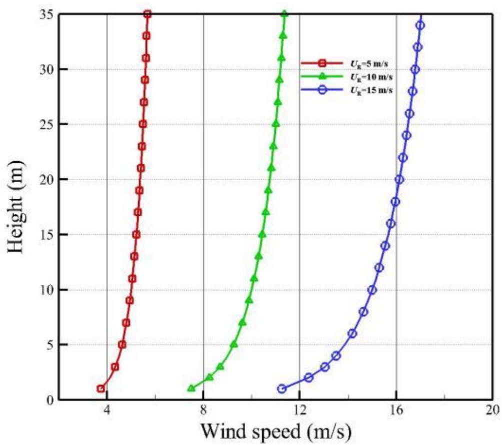

Figure 5. Mathematical model of wind gradient under different reference wind speeds (h_R = 10 m, h_0 = 0.001 m).

2.2. Logarithmic Mathematical Model of Wind Gradient [25]

The mathematical model of wind gradient at the sea surface can also be expressed by an exponential function:

$$U = U_R \left(\frac{h}{h_R}\right)^p \tag{7}$$

$$\frac{\delta U}{\delta h} = p \frac{U_R}{h_R} \left(\frac{h}{h_R}\right)^{p-1} \tag{8}$$

where wind speed U is a function of height h. The reference wind speed U_R can be selected according to the reference height h_R, which defines the wind profile's overall gradient and average speed value. Generally, the wind speed at 10 m is selected as the reference wind speed, as shown in Figure 7.

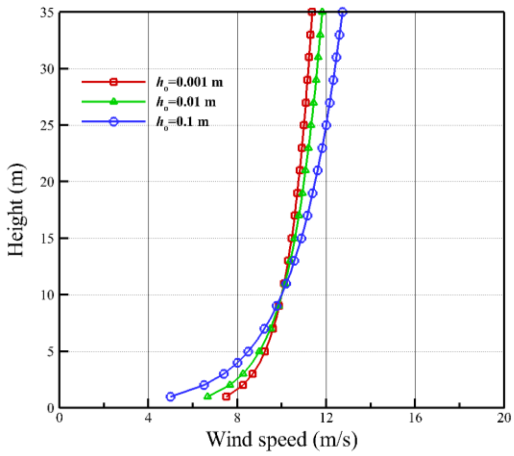

Figure 6. Mathematical model of wind gradient under different roughness factors (h_R = 10 m, U_R = 10 m/s).

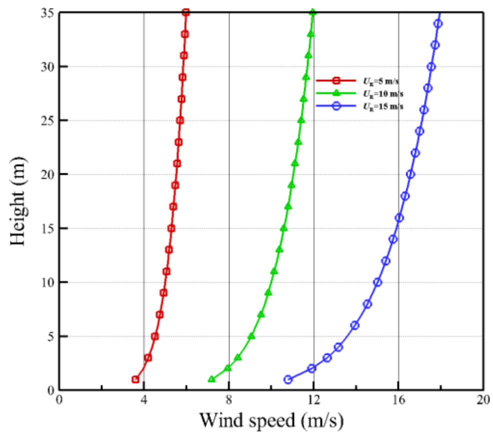

Figure 7. Mathematical model of wind gradient under different reference wind speeds (h_R = 10 m, p = 0.143).

Dietert [25] and Sachs [26] used the 1/7 law (p = 0.143) to describe the mathematical model of wind gradient at sea level. Of course, the value of p is not constant, and varies with roughness and other factors. The distribution of wind gradient along the spanwise height is shown in Figure 8.

2.3. Comparison of the Mathematical Models of Wind Gradient

It can be seen from Figures 5 and 7 that both mathematical models of wind gradient consider the distribution of wind speed and wind gradient along the spanwise direction, the wind gradient is larger at low altitudes, and the wind gradient changes more obviously with the increase of wind speed. It can be seen from Figures 6 and 8 that the wind gradient increases significantly at low altitudes with the increase of roughness factor and exponential factor. Therefore, the roughness factor and exponential factor can be considered as the key factors affecting the distribution characteristics of wind gradient.

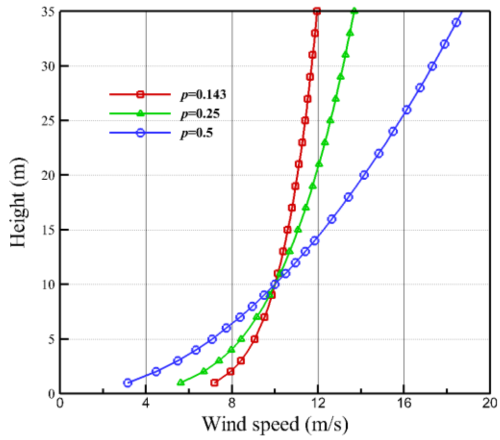

Figure 8. Mathematical model of wind gradient under different exponential parameters (h_R = 10 m, U_R = 10 m/s).

In this paper, the characteristic parameters of $p = 1/7$ and h_0 = 0.001 m were selected to compare the curves of the two wind gradient mathematical models at a wind speed of 10 m/s at a height of 10 m, as shown in Figure 9. It can be seen that the curves of the two mathematical models are relatively close to each other, and the wind speed values are slightly different with the increase of the spanwise height. However, there is no evidence that the wind gradient mathematical model is more suitable than the other to describe the wind speed in the atmospheric boundary layer. Therefore, these two mathematical models were chosen as the wind gradient mathematical models for the numerical experiments.

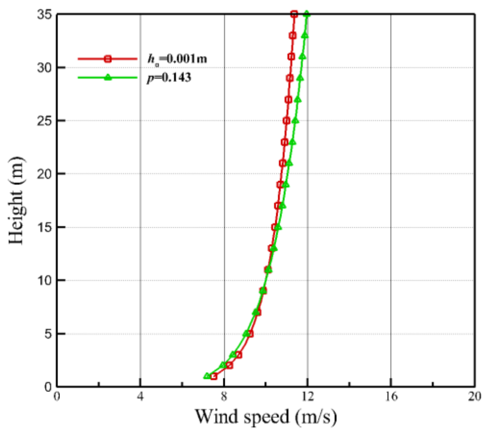

Figure 9. Comparison of two models of wind gradient under typical parameter settings.

According to Figure 9, the average speed of the wind calculation formula of the logarithmic mathematical model of wind gradient is derived as follows:

$$\overline{v} = \frac{\int_{h_1}^{h_2} U_R \frac{\ln h - \ln h_0}{\ln h_R - \ln h_0} dh}{h_2 - h_1} \tag{9}$$

Take h_R = 10 m, U_R = 10 m/s as an example, take h_0 = 0.001 m, and substitute Formula (9):

$$\overline{v} = \frac{\int_{h_1}^{h_2} 1.086 \ln(h) + 7.5 dh}{h_2 - h_1} \tag{10}$$

$$\overline{v} = \frac{\int_{h_1}^{h_2} U_R \left(\frac{h}{h_R}\right)^p dh}{h_2 - h_1} \tag{11}$$

Take p = 0.143 and substitute it into Equation (11):

$$\overline{v} = \frac{\int_{h_1}^{h_2} 7.194(h)^{0.143} dh}{h_2 - h_1} \tag{12}$$

It is calculated that the average speed of the two models of wind gradient is 10 m/s at h_R = 10 m and U_R = 10 m/s. Therefore, we chose the logarithmic mathematical model of wind gradient as the wind field entrance condition for a follow-up study.

3. Model and Numerical Method

3.1. Model of Wingsail

Drawing on the geometric parameters of wingsails designed by Li [2] for reference, three-dimensional modeling of the wingsail was carried out, and the wingsail layout on the ship is shown in Figure 10. The height from the bottom edge of the wingsail to the deck of the ship is 7 m to ensure aerodynamic forces. In the wingsail model, the position of the flap rotation axis is 90%c_1, the relative width of the gap is taken as 2.4%c_1, the ratio of the flap to total chord length is taken as 0.4, the total chord length is 3.5 m, and the aspect ratio is taken as 2. The flap deflection angle rotates within the range of 0°–25°. When the incoming wind speed is 10 m/s, its Reynolds number is

$$\mathrm{Re} = \frac{\rho U_R c}{\mu} = 2.4 \times 10^6 \tag{13}$$

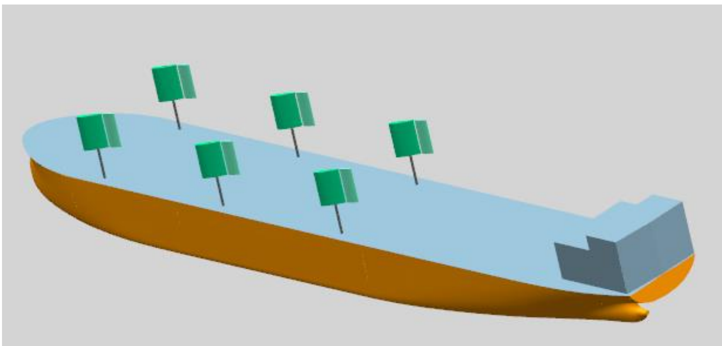

Figure 10. Schematic diagram of a certain height from the root of wingsails to the deck.

3.2. Computing Domain and Grid

Based on the operating characteristics of the two-element wingsail, the computational domain rectangular (32c × 30c × 10c) is determined as shown in Figure 11. Considering that the stall problem of the wingsail in the wind gradient state is discussed in this paper, the boundary conditions on the bottom surface of the computational domain are set to the standard no-slip solid wall. The inlet, left and right boundaries and upper boundary of the computational domain are set to the velocity inlet. The curve of the inlet velocity along the height by UDF is customized. The outlet boundary condition is set to a pressure outlet with a pressure magnitude equal to the far field pressure, and the wingsail surface is set to a no-slip solid wall.

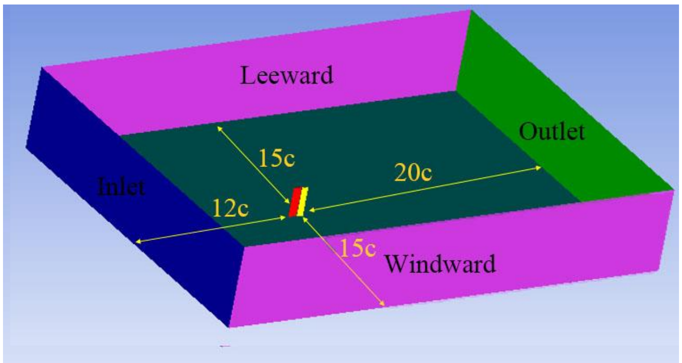

Figure 11. Calculation domain of a two-elements wingsail.

An unstructured grid was used to mesh the computational domain model by ANSYS ICEM. To control the total amount of the grid, the grid of the area near the two-element wingsail is encrypted, while the far region uses a larger grid size. Figure 12 shows the mesh details of the wingsail surface. Three different grid sizes (coarse grid, finer grid, and thinnest grid) are chosen to evaluate the grid sensitivity of the wingsail, which are shown in Table 1. The thinnest grid size of the wingsail surface is set to 0.25%c. The growth rate of the boundary layer grid is 1.05, and the number of boundary layers is 15. The y value is calculated as $1.5 \times 10^{-5}c$ to ensure that the y^+ value is less than 1, which is shown in Figure 13.

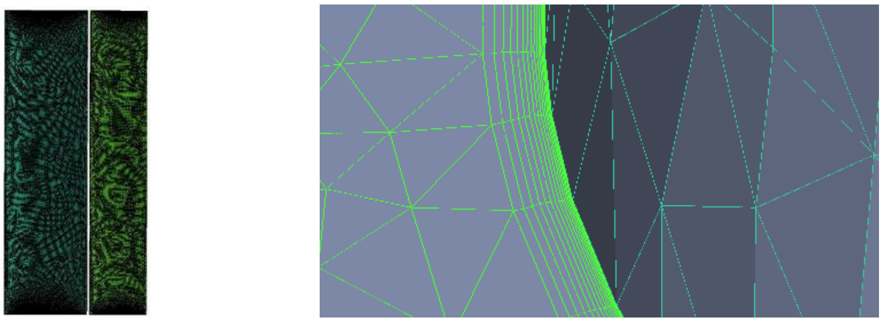

(**a**) (**b**)

Figure 12. Mesh details of wingsail surface. (**a**) Wingsail surface grid structure. (**b**) Boundary layer grid of the two-elements wingsail.

Table 1. Setting of wingsail surface grid parameters.

Grid Type	Grid Size of Wingsail Surface	Total Number of Grids
Coarse grid	0.8%c	1.045×10^7
Finer grid	0.4%c	1.453×10^7
Thinnest grid	0.25%c	1.883×10^7

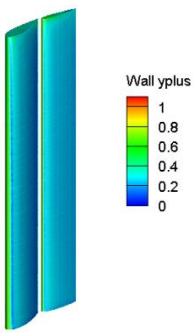

Figure 13. Cloud of y^+ on the surface of the wingsail at α = 6°.

To ensure that the number of grids have no effect on the performance of the two-element wingsail, the grid sensitivity is estimated for three grid models with different grid sizes at Reynolds number $Re = 2.4 \times 10^6$. The lift-drag characteristics are shown in Table 2. The lift and drag coefficient curves show monotonic convergence ($0 < R_G < 1$) during the numerical calculation.

Table 2. Grid sensitivity analysis at $\alpha = 6°$.

Type	ID	C_L	Error (%)	C_D	Error (%)
Thinnest grid	φ_1	1.8210	—	0.1516	—
Finer grid	φ_2	1.8216	0.033	0.1513	−0.1979
Coarse grid	φ_3	1.8193	−0.093	0.1522	0.3958
R_G	—	0.2826	—	0.3113	—

Finally, the grid convergence index (GCI) method is used to evaluate the three grid dispersion errors [27]. As can be seen from Table 3, the results of the solutions for C_L and C_D are 0.669% and 0.362%, respectively. The increase in the number of grids makes the variation in the lift-drag characteristics of the two-element wingsail small when a finer grid size is chosen. The thinnest grid types enable a more accurate calculation but with an increased computational cost. Therefore, when discussing the wingsail grid model, it is more appropriate to choose a finer mesh size (14.53 million) for the numerical simulation solution from the perspective of aerodynamic reliability.

Table 3. The calculated value of the dispersion error of C_L and C_D.

Parameter	C_L	C_D
r_{32}	2.05	2.05
r_{21}	1.63	1.63
φ_1	1.8210	0.1516
φ_2	1.8216	0.1513
φ_3	1.8193	0.1522
φ_4	1.8185	0.1525
p	2.531	3.3679
${\varphi_{ext}}^{21}$	0.2742	0.1408
${e_a}^{21}$	0.528%	0.453%
${e_{ext}}^{21}$	0.613%	0.227%
${GCI_{fine}}^{21}$	0.669%	0.362%

3.3. Verification of Numerical Methods

Since our research concerned the complex three-dimensional radial flow on the surface of a two-element wingsail at low and medium Reynolds numbers, the research results of Fiumara [14] on the AC72 airfoil were chosen for comparison. The transition SST turbulence model with correction was used to analyze the accuracy of our numerical method in terms of the performance of the three-dimensional model of a two-element wingsail and the prediction of the flow field.

The AC72 was the sail used in the 35th America's Cup. Fiumara et al. conducted experiments on a 1/20-scale model of the AC72 sail in an open return wind tunnel at the University of Toulouse, France, in 2015, and obtained more detailed experimental data, including the lift-drag characteristic curves and flow field. The design framework and experimental model of the wind tunnel experiments are shown in Figure 14. The duct has an elliptical shape of 3 m × 2 m. Pressure ports have been set on three sections of the main element (respectively) located at 25, 50 and 75% of the wingspan. The experimental Reynolds number of this model is low, and there is also a more obvious slot jet phenomenon on the sail surface, so this used by us for the calibration of numerical calculation; its design parameters are shown in Table 4. To ensure the accuracy of the numerical calculation method, the grid division of the computational domain of the AC72 was the same as that of the two-element wingsail model in the paper. The numerical schemes used SIMPLE, and the degree of accuracy of the numerical schemes used the second order upwind. The calculation software was ANSYS FLUENT.

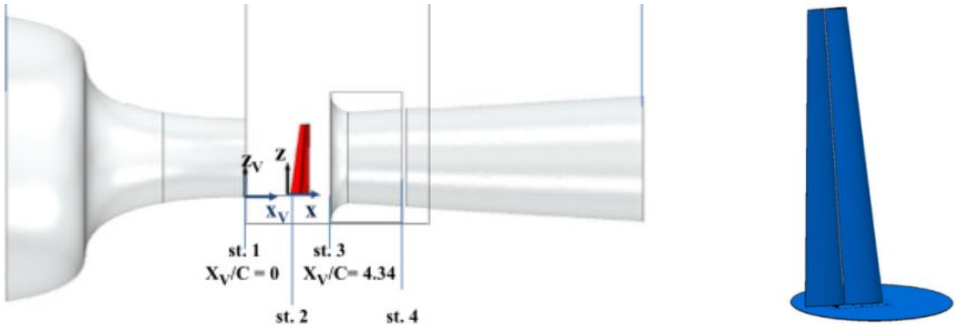

(**a**) (**b**)

Figure 14. Design framework and experimental model of the AC72 wingsail wind tunnel experiment. (**a**) Design Framework of the AC72 wingsail experiment. (**b**) AC72 wingsail experimental model.

Table 4. Design parameters of AC72 wingsail model.

Height	1.8 m
Total chord length of blade root	0.5 m
Reynolds number of blade root	6.4×10^5
Reynolds number of the blade tip	2.9×10^5
Gap width	6 mm
Flap rotation axis position	$95\%c_1$
Flap deflection angle	0–25°
Angle of attack	0–16°
The maximum speed in the duct	42 m/s
The airfoil of the main wing	NACA0025
The airfoil of the flap	NACA0012

The pressure coefficient of the different sections of AC72 is shown at a flap deflection angle of 15°, and an angle of attack of 0°, as shown Figure 15. It can be seen that the simulation and test results of the pressure load distribution of the main wing are relatively consistent in sections of z/h = 0.5 and z/h = 0.75.

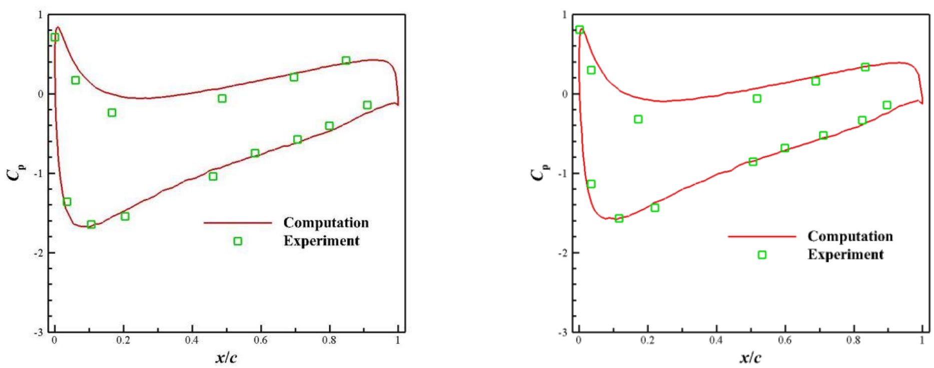

(**a**) (**b**)

Figure 15. Pressure coefficient of main wing in different sections of the AC72 wingsail. (**a**) z/h = 0.5, (**b**) z/h = 0.75.

The transition positions and separation bubble lengths of the suction surface of AC72 are listed in Table 5. It can be seen that the transition positions and separation bubble lengths for the AC72 predicted by the numerical simulation method are basically within 15% error compared to the experimental results. This indicates that it is feasible to use the transition SST turbulence model to predict the flow field of the 3D wingsail, and the results by numerical simulation method are acceptable.

Table 5. Transition position and separation bubble length of suction surface of AC72.

	Separation Position of Separation Bubble(/% c_1)			Length of Separation Bubble (/% c_1)		
	CFD	TEST	Error	CFD	TEST	Error
$z/h = 0.25$	34	39.5	−13.92%	14	12.5	12%
$z/h = 0.5$	30	32	−6.25%	18	16	12.5%
$z/h = 0.75$	31	36	−13.89%	17	15	13.33%

4. Result

4.1. Effect of Angle of Attack on the Aerodynamic Characteristics of the Wingsail

Figure 16 shows the lift-drag characteristic curves of the two-element wingsail for uniform wind and logarithmic gradient wind conditions. From Figure 16, it can be seen that the stall angle of the two-element wingsail is increased and the maximum lift coefficient is increased by 8.6% compared with the uniform wind condition, while the drag coefficient is reduced. This indicates that the stall delay phenomenon occurs in the two-element wingsail under the effect of gradient wind and the maximum lift coefficient is increased. It is helpful to maintain the stability of the aerodynamic performance of the two-element wingsail under the gradient wind condition.

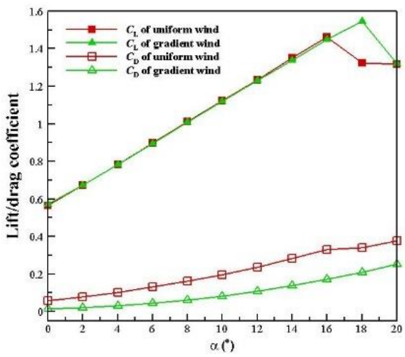

Figure 16. Lift-drag characteristic of the wingsail under mean wind and gradient wind conditions.

Figure 17 shows the limiting streamline of the wingsail in the near-stall angles under uniform wind and gradient wind conditions. From Figure 17, it can be seen that at an angle of attack of 16°, there is no flow separation on the suction surface of the wingsail in both uniform and gradient winds. At an angle of attack of 18°, two separating vortices appear on the suction surface of the main wing under the uniform wind condition, and cause a large-scale backflow on the suction surface of the flap, which causes a deep stall of the wingsail, while the suction surface of the main wing under the gradient wind condition only shows a small-scale flow separation, which causes a light stall of the wingsail while maintaining a high lift coefficient. This effectively verifies the delayed stall phenomenon under the gradient wind condition.

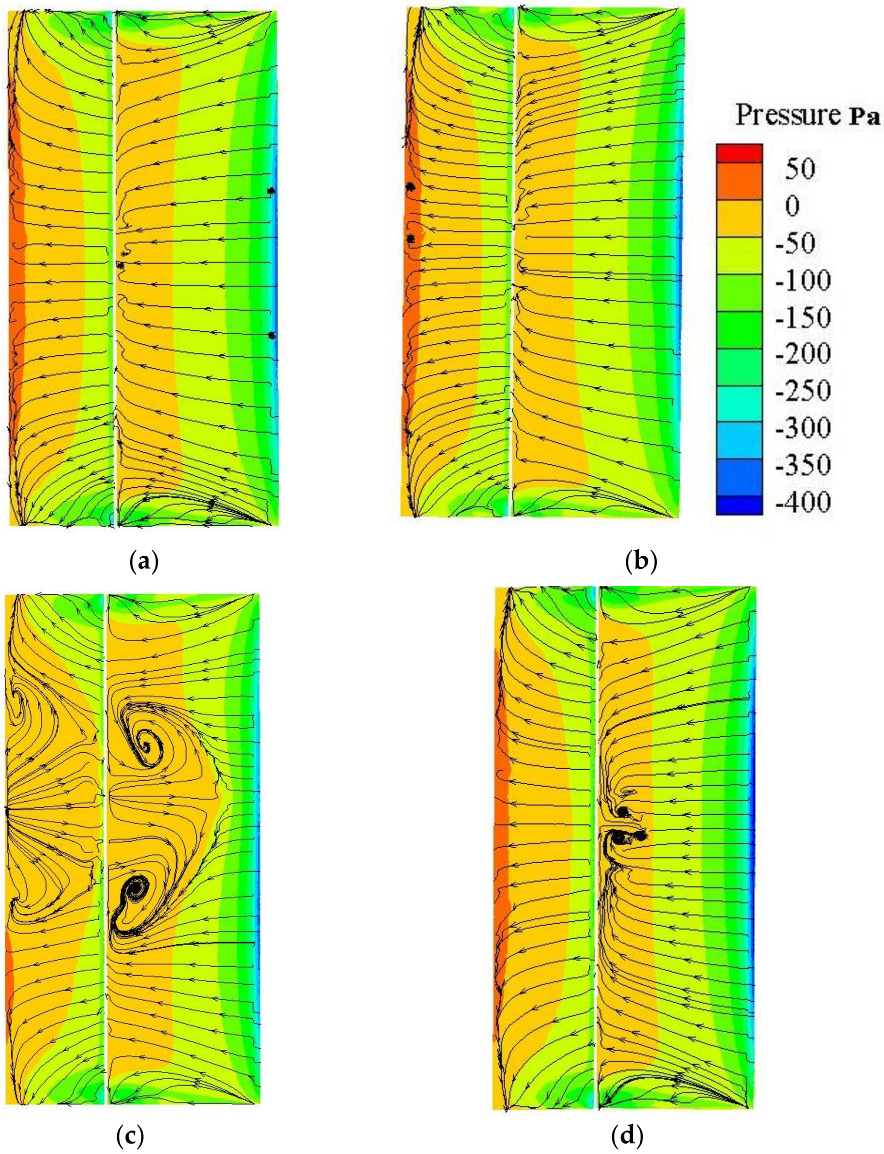

Figure 17. Wall limiting streamline of the wingsail under uniform wind and gradient wind conditions. (**a**) Uniform wind at $\alpha = 16°$. (**b**) Gradient wind at $\alpha = 16°$. (**c**) Uniform wind at $\alpha = 18°$. (**d**) Gradient wind at $\alpha = 18°$.

Figure 18 shows the velocity cloud of the wingsail at near-stall angles. It can be seen from Figure 18a that a low-velocity zone exists in the middle of the suction surface of the wingsail under uniform wind conditions at the angle of attack of 18°, which is caused by flow separation, while the flow velocity distribution of the main wing suction surface in Figure 18b is uniform, and there is no low-pressure zone under the gradient wind conditions. With the increase of the angle of attack, the low-velocity region in the main wing suction surface expands under the uniform wind condition, as seen in Figure 18c. The low-velocity zone also appears in the middle of the suction surface of the main wing under the gradient wind condition, and the stall of the wingsail develops faster, as shown in Figure 18d.

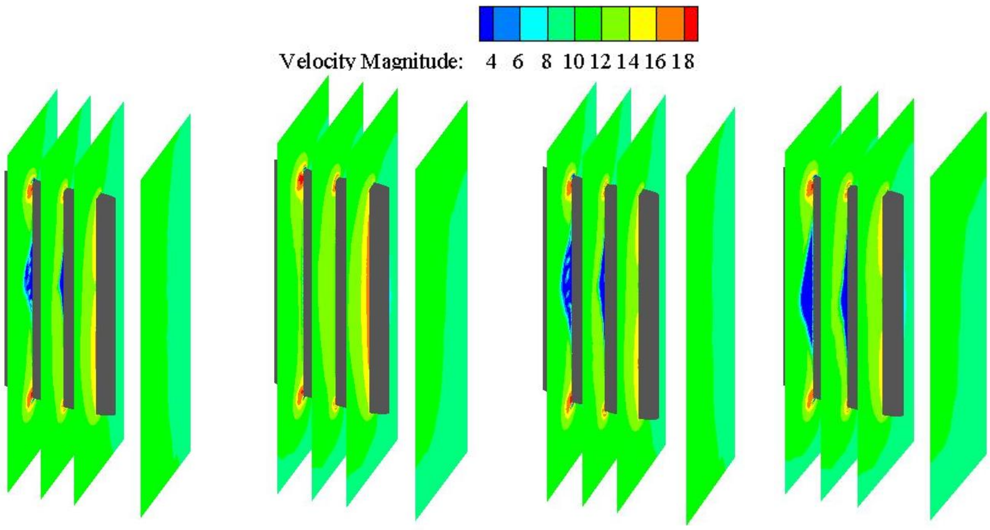

Figure 18. Velocity distribution of a two-element wingsail under uniform wind and gradient wind conditions. (**a**) Case 3 with uniform wind at α = 18°. (**b**) Case 3 with gradient wind at α = 18°. (**c**) Case 3 with uniform wind at α = 20°. (**d**) Case 3 with gradient wind at α = 20°.

To verify the analysis in Figure 16, the three-dimensional streamline of the wingsail at the angle of attack of 18° and 20° was also drawn, as shown in Figure 19. From Figure 19a, it can be seen that there is a large-scale separation vortex in the middle of the main wing suction surface under the uniform wind condition at an angle of attack of 18°, which is mainly caused by the return flow of the airflow through the gap. However, in Figure 19b, the flow separation on the suction surface of the main wing is not obvious. This is because, under the effect of wind gradient, the spanwise velocity along the height of the wingsail gradually increases, which produces an acceleration pointing to the direction of the top of the blade on the suction side of the wingsail. At this time, external airflow comes to supplement the airflow flowing toward the top of the blade, which makes the separation vortex that should exist under uniform wind conditions compressed, delaying the stall of the wingsail. In Figure 19c, as the angle of attack increases under the uniform wind, the separation vortex on the suction surface of the main wing expands and forms two basically symmetrical vortices. The large-scale flow separation also occurs in the wingsail in Figure 19d. Although the scale of its vortex is smaller than that of the vortex in Figure 19c, the stall develops faster under the gradient wind condition. This indicates that whether it is a uniform wind condition or a gradient wind condition, a small fluctuation in the angle of attack in the near-stall angles may cause a deep stall, which leads to a rapid reduction in the lift, which should be avoided in engineering applications.

4.2. Effect of Flap Deflection Angle on Aerodynamic Characteristics of Wing Sails

The mechanism of the effect of flap deflection angle on the stall of the wingsail was analyzed under gradient wind conditions. Figure 20 shows the curve of the lift/drag coefficient of the wingsail with the flap deflection angle at an angle of attack of 16°. From Figure 20, it can be seen that in the near-stall angles, the lift coefficient increases slowly and then decreases sharply as the flap deflection angle increases, reaching a maximum value at the flap deflection angle of 23°, when the drag coefficient is also the maximum. This shows that a small change with the flap deflection angle in the near-stall angles may trigger a stall of the wingsail and cause a sharp drop in the lift, which is more obvious under uniform wind conditions.

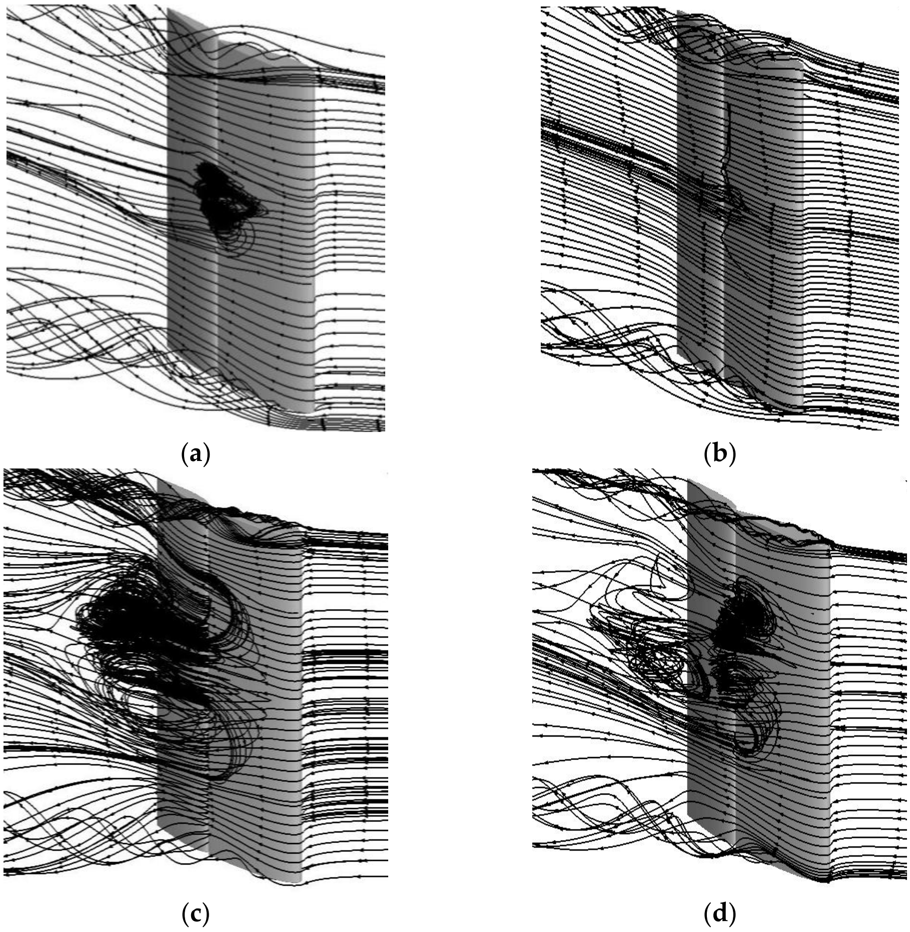

Figure 19. Three-dimensional streamline of a two-element wingsail under uniform wind and gradient wind conditions. (**a**) Case 3 with uniform wind at α = 18°. (**b**) Case 3 with gradient wind at α = 18°. (**c**) Case 3 with uniform wind at α = 20°. (**d**) Case 3 with gradient wind at α = 20°.

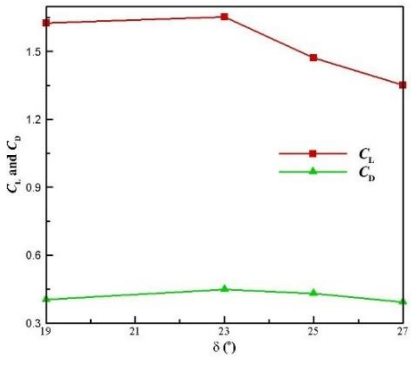

Figure 20. Curve of lift/drag coefficient vs. flap deflection angle in stall angles.

Figure 21 shows the two-dimensional streamline of the wingsail at flap deflection angles of 19°, 23°, 25°, and 27°, which demonstrate the flow separation process on the surface of the two-element wingsail under the gradient wind condition. From Figure 21, in the section of 0.9*h*, the flow separation at the trailing edge of the flap occurs at a flap deflection angle of 23°, and the separation vortex at the trailing edge of the flap is also relatively small at the flap deflection angle of 27°. However, in the section of 0.65*h*, the flow separation of the flap surface at a flap deflection angle of 25° extends to the leading edge, while the flow separation of the main wing surface is smaller. It is not until the flap deflection angle increases to 27° that a clear separation vortex is seen at the trailing edge of the main wing, but it appears very flat compared to the large-scale vortex of the flap surface. In the section of 0.5*h*, at flap deflection angles of 19°, 23°and 25°, the vortex at the surface of the wingsail is similar to that in the section of 0.65*h*, and the light stall of the main wing ensures that the lift coefficient of the wingsail does not decrease significantly. When the flap deflection angle increases to 27°, a deep stall occurs in the main wing, resulting in a significant reduction in the lift coefficient. Overall, the flow separation of the wingsail under gradient wind conditions develops relatively quickly in the near-stall angles. Once a flat vortex is formed at the trailing edge of the wingsail, with the slow increase of the flap deflection angle, the flow separation rapidly extends to the entire surface of the wingsail and enters the deep stall state.

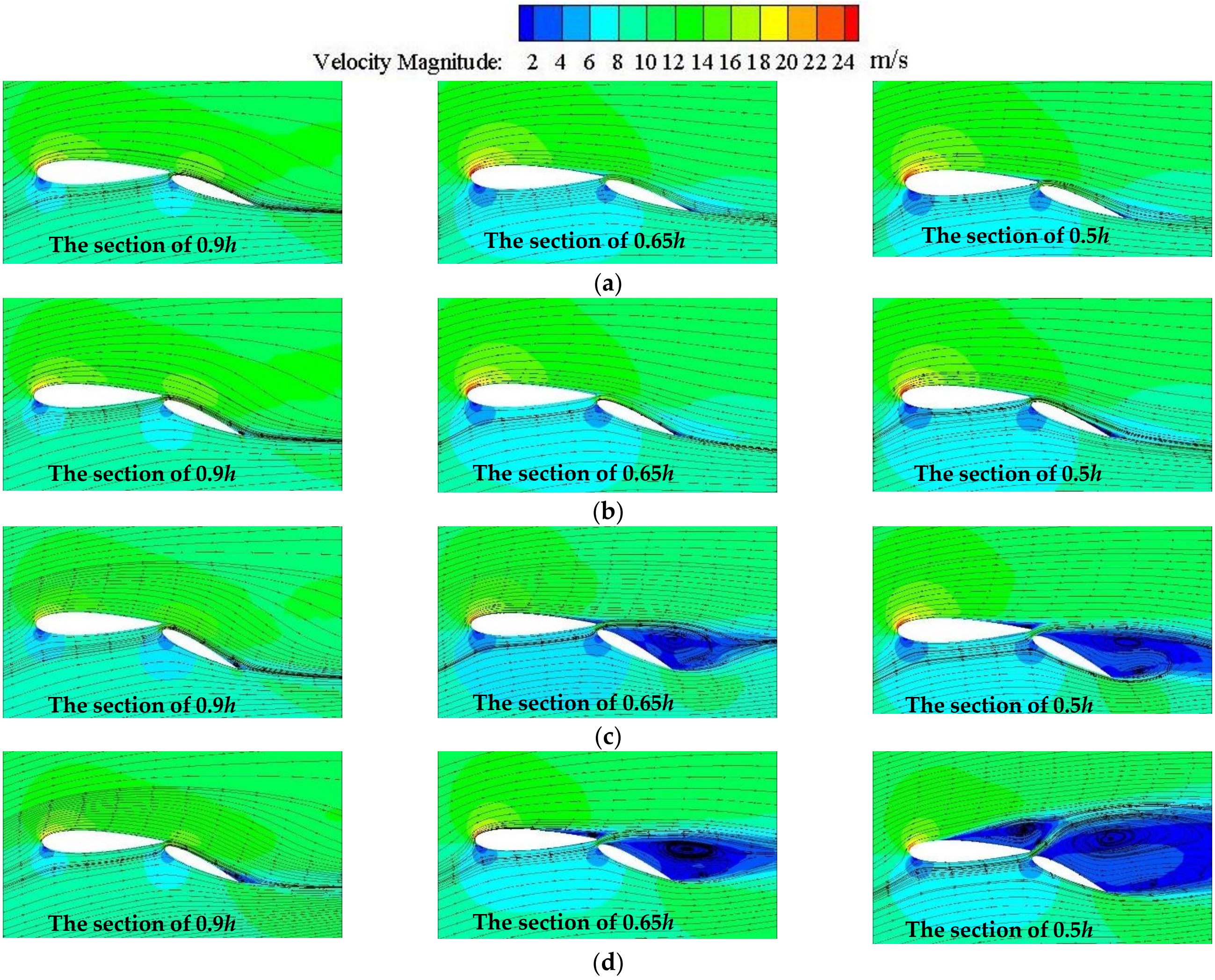

Figure 21. Streamline of the two-element wingsail under different flap deflection angles. (**a**) δ = 19°. (**b**) δ = 23°. (**c**) δ = 25°. (**d**) δ = 27°.

Figure 22 shows the three-dimensional streamlines of the two-element wingsail suction surface at an angle of attack of 16°. At flap deflection angles of 19° and 23°, the flow on the surface of the wingsail is an attaching flow, which is consistent with the streamline on the two-dimensional section. When the flap deflection angle increases to 25°, the flow enters the slight stall zone, which is separated at the trailing edge of the main wing above 1/3 of the height of the wingsail under the action of the wind gradient. Part of the streamline flows towards the top of the blade after entering the separation area of the main wing, showing three-dimensional flow characteristics. At this time, the vortex on the flap suction surface is obviously inclined to the middle and upper part of the wingsail, squeezed by the lower low-speed wind. As the flap deflection angle continues to increase, the vortex in the middle of the trailing edge of the main wing expands, and the large-scale vortex on the surface of the flap is also squeezed, which promotes the further development of stall.

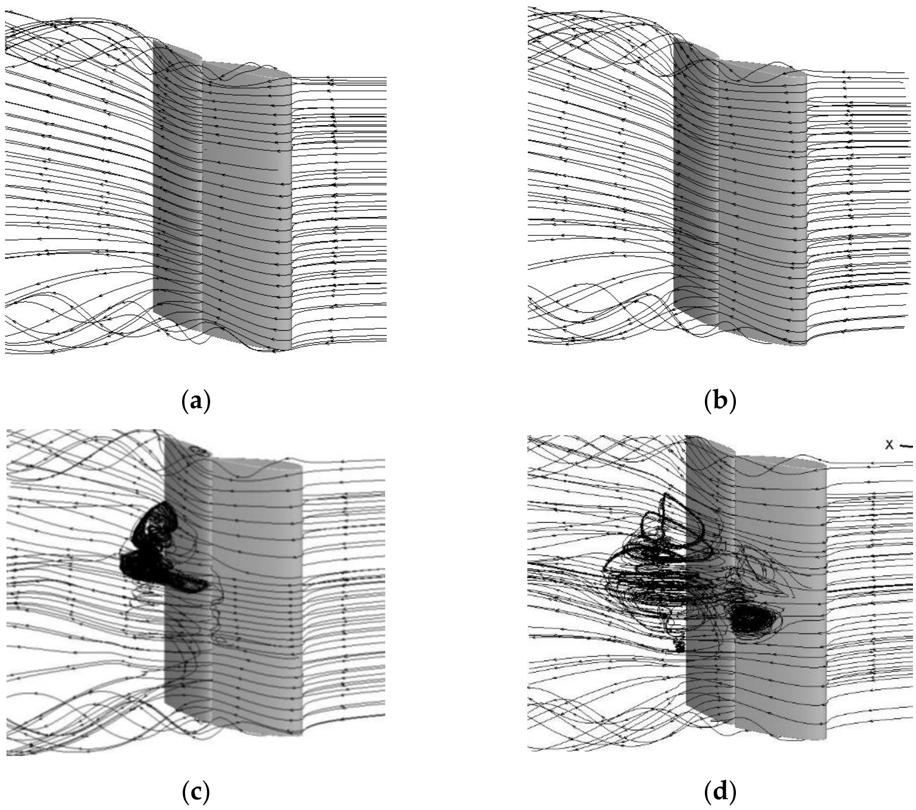

Figure 22. Three-dimensional streamline of the two-elements wingsail at angle of attack of 16°. (**a**) δ = 19°. (**b**) δ = 23°. (**c**) δ = 25°. (**d**) δ = 27°.

To further analyze the three-dimensional flow characteristics of the wingsail in the near-stall angles at high flap deflection angles, a three-dimensional flow line passing through the wingsail surface is shown as Figure 23 with an average wind speed of 10 m/s, an angle of attack of 16°, and a flap deflection angle of 25° under the gradient wind conditions.

The flow line starts from point A at the leading edge of the main wing and flows along the suction side of the main wing, and then flows backward the leading edge of the main wing at point B. At the same time, point B is also the turning point when the flow changes from a chordal direction to a spanwise direction. This is because when the air flows from point A to point B, due to the limited spanwise pressure brought by the gradient wind, it is not enough to resist the horizontal velocity to change the flow direction. However, at point B, the horizontal velocity of the air is zero, while the spanwise velocity is affected by the wind gradient. According to the law of mass conservation, it is easy to deflect the flow line from a horizontal direction to a spanwise direction under the action of spanwise pressure. Between point B and point C, the velocity component of the flow line in the horizontal direction points from the trailing edge of the main wing to the leading edge and enters the zone of the separated vortex. As the spanwise height increases, the spanwise pressure under the action of the wind gradient always exists. At the same time, under the action of horizontal velocity, the flow line flows spirally between points B-C-D at the top of the wingsail, and finally enters the leading edge of the flap at point D, flowing out from the vortex. The flow line between B-C-D is similar to the streamline under Coriolis force in the three-dimensional rotation effect and is also related to the actual flow situation.

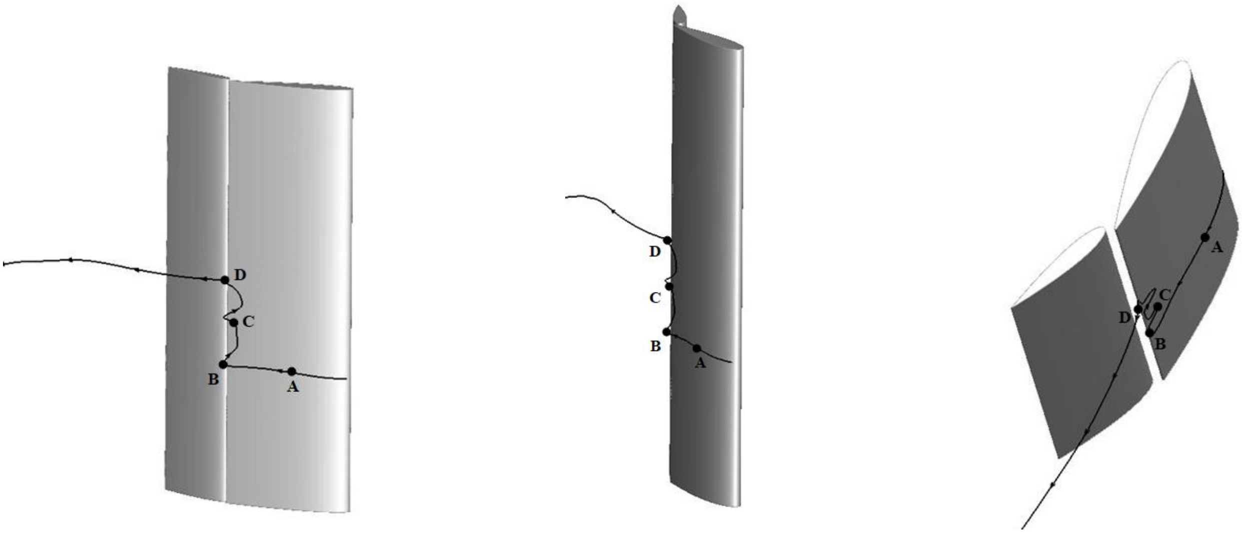

Figure 23. A three-dimensional streamline with flap deflection angle of 25° under gradient wind conditions.

4.3. Effect of Wind Speed on the Stall of the Two-Element Wingsail

The stall process of the wingsail was analyzed when the average wind speed increased from 6 m/s to 18 m/s under gradient wind conditions at the flap deflection angle of 25° and an angle of attack of 6°–14°. The wind speed distribution is shown in Figure 24, which shows that as the wind speed increases, the spanwise wind gradient increases with the increase of height.

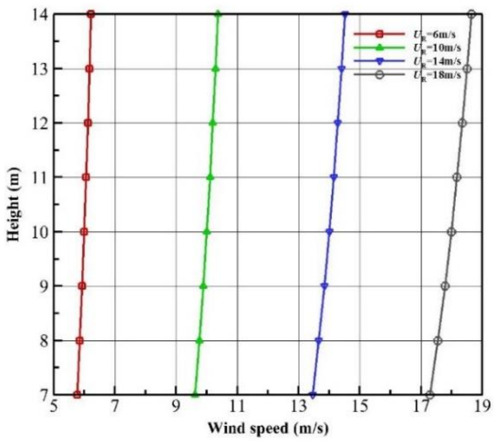

Figure 24. Mathematical models of wind gradient under different wind speeds (h_R = 10 m, h_0 = 0.001 m).

Figure 25 shows the curves of the lift coefficient of the two-element wingsail with an average wind speed under gradient wind and uniform wind conditions. From Figure 25a, it can be seen that at the angle of attack of 8°, the lift coefficient first increases and then decreases as the wind speed increases, where the lift coefficient with an average wind speed of 18 m/s decreases sharply, indicating that the wingsail has seriously stalled at this time. As the angle of attack increases, the lift coefficient with average wind speeds of 6, 10, and 14 m/s also increases and then decreases, and reaches a maximum at an angle of attack of 10°. By comparing the lift coefficients with the uniform wind condition in Figure 25b, it can be seen that the lift coefficient in the gradient wind condition is higher at the range of 8°−12°, and the lift coefficients decrease less after the stall occurs, which indicates that the gradient wind improves the stall phenomenon of the two-element wingsail.

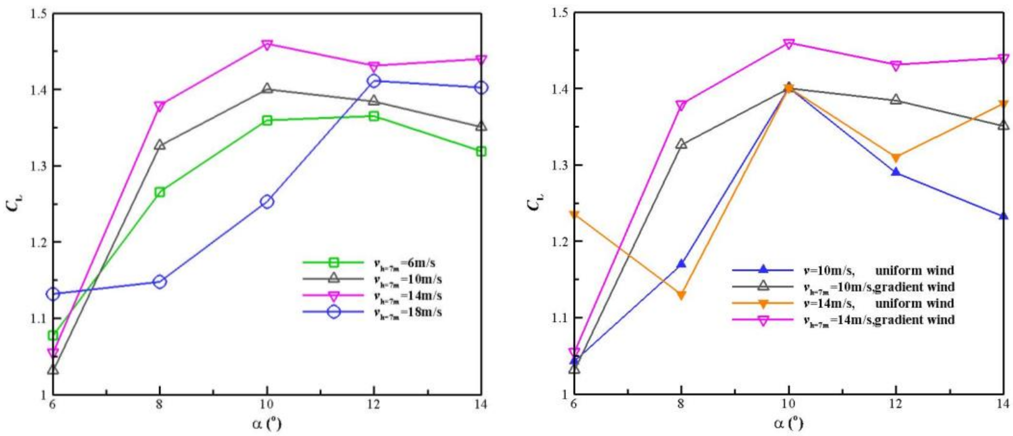

(**a**) (**b**)

Figure 25. Curve of lift coefficient with wind average speed under different conditions. (**a**) Conditions of gradient wind. (**b**) Conditions of gradient wind and uniform wind.

The following is an analysis of the flow field of the wingsail at different average wind speeds, taking an angle of attack of 10° as an example; Figure 26 shows the limiting streamline at different average wind speeds. From Figure 26, it can be seen that when the average wind speed is 6 m/s, due to the small spanwise wind gradient, it can be regarded as a uniform wind, and there are two symmetrically separated vortex structures in the middle of the flap suction surface. Although the flap has stalled at this time, the overall lift coefficient of the wingsail is kept at a high position because the streamline of the main wing suction surface is not separated. As the average wind speed increases to 10 m/s, the symmetrical vortex in the middle of the flap suction surface is squeezed, and the pressure distribution at the trailing edge of the main wing is more uniform. Therefore, the stall is suppressed, and the lift coefficient is improved. As the average wind speed further increases to 14 m/s, the separation vortex of the flap increases again. Since the spanwise wind gradient is also increasing at this time (see Figure 26), according to the delayed stall principle of gradient wind (see Figure 25), the lift coefficient of the wingsail is still increasing at this time. Until the average wind speed increases to 18 m/s, due to the flap suction surface appearing with multiple separation vortexes, the flap has a deep stall and the lift coefficient of the wingsail is significantly reduced.

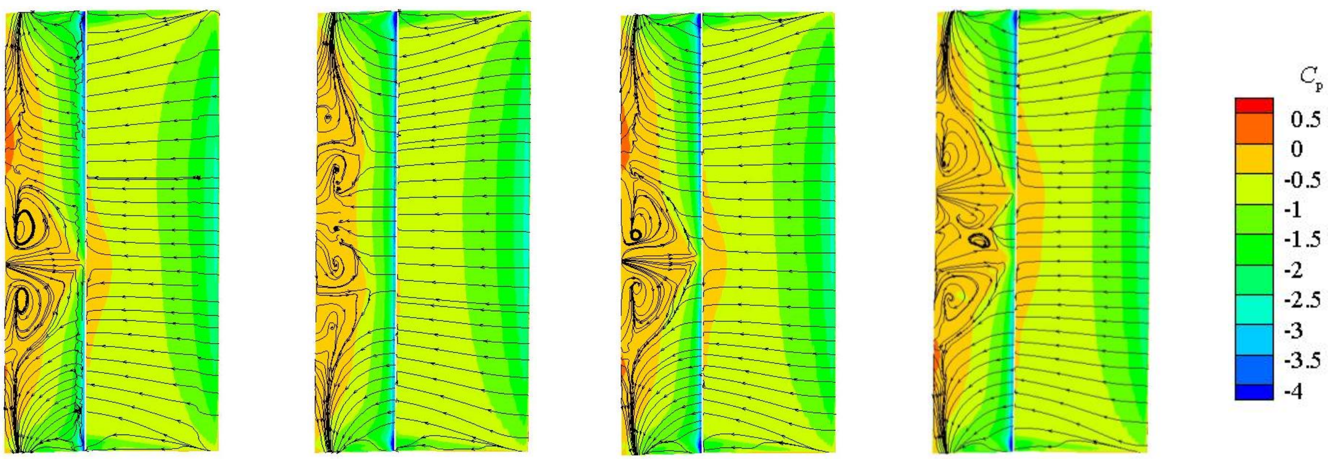

(**a**) (**b**) (**c**) (**d**)

Figure 26. Limiting streamline of the wingsail under different average wind speeds. (**a**) v = 6 m/s. (**b**) v = 10 m/s. (**c**) v = 14 m/s. (**d**) v = 18 m/s.

Figure 27 shows the speed cloud of the wingsail under different average wind speeds in the near-stall angles. It can be seen from Figure 27 that when the average wind speed is 6 m/s, there is a low-speed zone with a wide distribution on the flap suction surface, and it expands toward the wake direction. With the average wind speed increasing, the low-speed zones are gradually squeezed into two low-speed zones. When the average wind speed reaches 14 m/s, the low-speed zone becomes very flat and gradually disappears in the wake, while the lift coefficient is at its highest. This indicates that the increase in the average speed of the gradient wind delays stall and improves the lift coefficient to a certain extent. However, when the average wind speed increases to 18 m/s, the flaps have long been severely stalled, which requires strict control of the available wind speed range to ensure the reliability of its wind load.

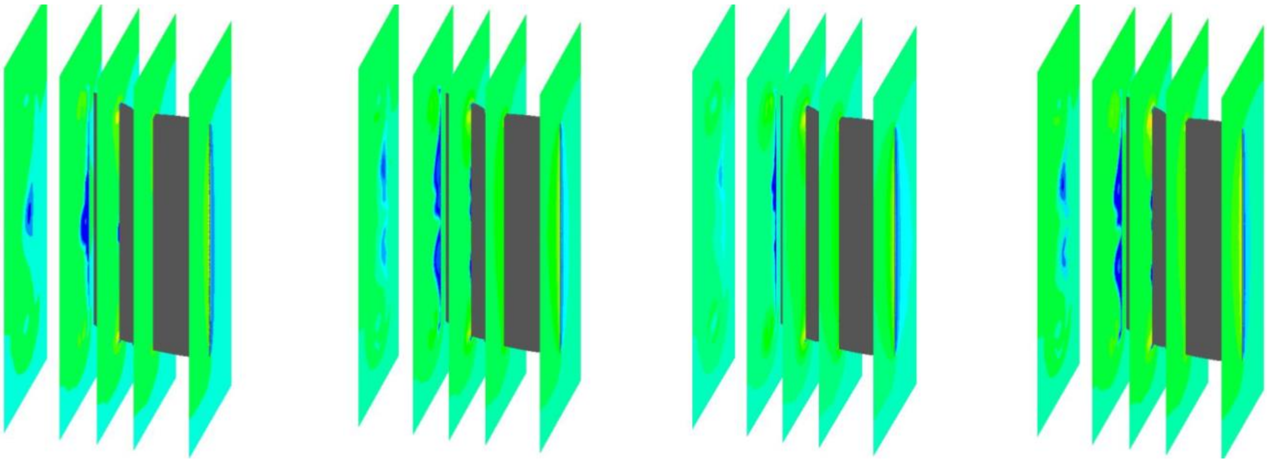

(**a**) (**b**) (**c**) (**d**)

Figure 27. Speed cloud of wingsail at different average wind speeds at α = 10°. (**a**) v = 6 m/s. (**b**) v = 10 m/s. (**c**) v = 14 m/s. (**d**) v = 18 m/s.

5. Conclusions

It is very important that sails for ship-assisted propulsion work well under gradient wind conditions in the atmospheric boundary layer. In order to study the aerodynamic characteristics of the wingsail in the atmospheric boundary layer above sea level, a transition SST turbulence model is used for numerical simulation of the wingsail model with uniform wind and gradient wind conditions, and the following conclusions are drawn.

1. The wind gradient can delay the stall caused by the increased angle of attack. This is because the airflow on the suction surface of the wingsail in the spanwise wind direction exerts an acceleration towards the top of the wingsail. At the same time, the supplementary airflow compresses the separated vortex, thus delaying the stall of the two-element wingsail.

2. Under gradient wind conditions, the flow separation of the wingsail develops rapidly in the near-stall angles. Once a flat separation vortex is formed at the trailing edge of the wingsail, with the slow increase in the flap deflection angle, the flow separation rapidly expands to the entire surface of the wingsail and a deep stall occurs. Therefore, the small change of the flap deflection angle in the near-stall angles may lead to stall of the wingsail, which should be avoided in engineering applications.

3. The increase in the average speed of gradient wind delays stall and improves the lift coefficient to a certain extent. However, when the average wind speed increases to 18 m/s, the flaps have already seriously stalled, which requires strict control of the available wind speed range to ensure the reliability of its wind load.

Author Contributions: Conceptualization, C.L. and H.W.; investigation, C.L. and H.W.; methodology, C.L. and P.S.; software, C.L.; writing—original draft preparation, C.L.; writing—review and editing, H.W.; supervision, P.S. All authors have read and agreed to the published version of the manuscript.

Funding: This research was funded by General Project of Natural Science Research in Jiangsu Universities, 20KJB580008.

Institutional Review Board Statement: Not applicable.

Informed Consent Statement: Not applicable.

Data Availability Statement: The data presented in this study are available on request from the corresponding author. The data are not publicly available due to Limitations of the study phase.

Conflicts of Interest: The authors declare no conflict of interest.

Nomenclature

Re	Reynolds number [-]
α	Angle of attack of the wingsail (AOA) [°]
c	Total chord of the wingsail [m]
c_1	Chord of the main wing [m]
C_D	Drag coefficient [-]
C_L	Lift coefficient [-]
δ	Flap deflection angle [°]
g	non-dimensional slot width (g/c_1) [-]
y^+	Non-dimensional wall distance [-]
ρ	The density of the air [kg/m^3]
z	The height of wingsail in the vertical direction [m]
h	Wingsail height [m]
L	Lift force [N]
D	Drag force [N]
v	The velocity of inflow [m/s]
h_0	The roughness factor [m]
p	The exponential factor [-]

References

1. AYRO Raises €10.5M to Boost Development of Wingsail Technology [EB/OL]. Available online: https://vpoglobal.com/2021/09/17/AYRO-RAISES-E10-5M-TO-BOOST-DEVELOPMENT-OF-WINGSAIL-TECHNOLOGY/.2021-09-17 (accessed on 5 March 2022).
2. Li, C.; Wang, H.; Sun, P. Numerical Investigation of a Two-Element Wingsailfor Ship Auxiliary Propulsion. *Mar. Sci. Eng.* **2020**, *8*, 333. [CrossRef]
3. Borzacchiello, R.G. Fatigue Approach for WAPS. Master's Thesis, West Pomeranian University of Technology, Szczecin, Poland, 2021.
4. Ouchi, K.; Uzawa, K.; Kanai, A. "Wind Challenger" the Next Generation Hybrid Sailing Vessel. In Proceedings of the Third International Symposium on Marine Propulsors SMP'13, Launceston, TAS, Australia, 5–8 May 2013.
5. Wu, J. Laboratory studies of wind-wave interactions. *Fluid Mech.* **1988**, *34*, 91–122. [CrossRef]
6. Lenschow, D.H. Preliminary Results from the Air Mass Transformation Experiment (AMTEX). *Bull. Am. Meteorol. Soc.* **1976**, *57*, 1346–1355. [CrossRef]
7. Li, Q.; Zhi, L.; Hu, F. Boundary layer wind structure from observations on a 325m tower. *J. Wind. Eng. Ind. Aerodyn.* **2010**, *98*, 818–832. [CrossRef]
8. Sánchez-García, R.; Gomez, R.; Escobar, A. Wind Response of a Bridge Pylon Using Numerical Simulations of the Atmospheric Boundary Layer and Fluid Structure Interaction (FSI). *Dev. Int. Bridge Eng.* **2021**, *28*, 255–261.
9. Hu, H.; Yang, Z.; Sarkar, P. Dynamic wind loads and wake characteristics of a wind turbine model in an atmospheric boundary layer wind. *Exp. Fluids.* **2012**, *52*, 1277–1294.ok. [CrossRef]
10. Liu, D.-N.; Hou, Z.-X.; Guo, Z.; Yang, X.-X.; Gao, X.-Z. Permissible Wind Conditions for Optimal Dynamic Soaring with a Small Unmanned Aerial Vehicle. *CMES Comput. Model. Eng. Sci.* **2016**, *111*, 531–565.
11. Daniel, W.A. The CFD Assisted Design and Experimental Testing of a Wingsail with High Lift Device. Ph.D. Thesis, University of Salford, Salford, UK, 1996.
12. Blakeley, A.; Flay, R.; Richards, P. Design and Optimisation of Multi-Element Wing Sails for Multihull Yachts. In Proceedings of the 18th Australasian Fluid Mechanics Conference, Launceston, TAS, Australia, 3–7 December 2012.

13. Chapin, V.; Gourdain, N.; Verdin, N. Aerodynamic Study of a Two-Elements Wingsail for High Performance Multihull Yachts. In Proceedings of the 5th High Performance Yacht Design Conference, Auckland, New Zealand, 10–12 March 2015.
14. Fiumara, A.; Gourdain, N.; Chapin, V. Numerical and experimental analysis of the flow around a two-element wingsail at Reynolds number 0.53×10^6. *Int. J. Heat Fluid Flow* **2016**, *62*, 538–551. [CrossRef]
15. Wen-Rong, H.; Hong-Biao, Z.; Zu-Rong, D. Computational Study of theAerodynamicsof Sailsin aTwisted Wind. *J. Shanghai Jiaotong Univ.* **2008**, *42*, 1900–1903. (In Chinese)
16. Mortimer, I. A comparison of downwind sail coefficients from tests in different wind tunnels. *Ocean. Eng.* **2014**, *90*, 62–71.
17. Thuillier, R.; Lappe, U. Wind and Temperature Profile Characteristics from Observations on a 1400 ft Tower. *J. Appl. Meteorol.* **1964**, *3*, 299–306. [CrossRef]
18. Ricardo, B.; Anouck, G.; Mariam, A.; Joo, S. Shear Wind Estimation. In Proceedings of the AIAA Guidance, Navigation, and Control Conference, American Institute of Aeronautics and Astronautics, Portland, OR, USA, 8–11 August 2011.
19. Burton, W.V. Wind Tunnel Simulation of an Atmospheric Boundary Layer. Master's Thesis, Texas Tech University, Lubbock, TX, USA, 2001.
20. Holmes, D. Wind Loading of Structures. Spon Press: New York, NY, USA, 2001.
21. Tieleman, H.W.; Ge, Z.; Hajj, M.R.; Reinhold, T.A. Pressures on a surface-mounted rectangular prism under varying incident turbulence. *J. Wind. Eng. Ind. Aerodyn.* **2003**, *91*, 1095–1115. [CrossRef]
22. Bower, G.C. Boundary Layer Dynamic Soaring for Autonomous Aircraft Design and Validation. Ph.D. Thesis, Stanford University, Stanford, CA, USA, 2011.
23. Wang, H.; Zhang, Z.; Wu, H. Simulation of Arctic Surface Radiation and Energy Budget during the Summertime using the Single-Column Model. *Acta Oceanol. Sin.* **2008**, *27*, 1–12.
24. Sukumar, P.P.; Selig, M.S. Dynamic Soaring of Sailplanes Over Open Fields. *J. Aircr.* **2013**, *50*, 1420–1430. [CrossRef]
25. Deittert, M.; Richards, A.; Toomer, C.A.; Pipe, A. Engineless Unmanned Aerial Vehicle Propulsion by Dynamic Soaring. *J. Guid. Control. Dyn.* **2009**, *32*, 1446–1457. [CrossRef]
26. Sachs, G.; Bussotti, P. Application of Optimal Control Theory to Dynamic Soaring of Seabirds. In *Variational Analysis and Applications*; Giannessi, F., Maugeri, A., Eds.; Springer: New York, NY, USA, 2005; Volume 79, pp. 975–994.
27. Celik, I.B.; Ghia, U.; Roache, P.J.; Freitas, C.J. Procedure for estimation and reporting of uncertainty due to discretization in CFD applications. *J. Fluids Eng.* **2008**, *130*, 078001.

Disclaimer/Publisher's Note: The statements, opinions and data contained in all publications are solely those of the individual author(s) and contributor(s) and not of MDPI and/or the editor(s). MDPI and/or the editor(s) disclaim responsibility for any injury to people or property resulting from any ideas, methods, instructions or products referred to in the content.